SUPPLEMENTARY INFORMATION

On the near-wall accumulation of injectable particles in the microcirculation: smaller is not better

Tae-Rin Lee, Myunghwan Choi, Adrian M. Kopacz,

Seok-Hyun Yun, Wing Kam Liu, Paolo Decuzzi

Meshing parameters for the computational domain.

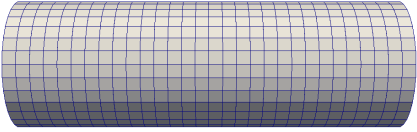**Supplementary Table S1** Meshing details for the RBC, NMP and capillary.

RBC meshing

number of nodes	938	
element type	Tetrahedral	
number of elements	4488	

Injectable particle meshing

number of nodes	892	
element type	Tetrahedral	
number of elements	4115	

Capillary meshing

number of nodes	4061	
element type	Hexahedral	
number of elements	3420	

Validation of the Immersed Finite Element Method for whole blood flow analysis. The Immersed Finite Element Method [1-3] for simulating the flow of whole blood in the microcirculation was validated using four different test cases (**Supplementary Fig. S1**), namely **a**) the analysis of RBC stretching under uniaxial tensile forces; **b**) the computation of the

discharge hematocrit out of a tube; **c**) the quantification of the apparent blood viscosity as a function of the RBC volumetric concentration; and **d**) the thickness of the cell free layer at different hematocrits. The computational predictions were compared with experimental data provided in the literature and the agreement was found to be very good, thus supporting the accuracy and validity of the proposed approach.

In the **Supplementary Fig. S1a**, a stretching test of RBC was performed to validate the large deformation of RBCs in the microvessel. The change in RBC diameter along the axial and transverse directions was numerically predicted and compared with experimental data, generated in optical tweezers-based stretching tests.[4] The RBC was modeled as described in the Method of this manuscript, using the parameters of **Table 1** and **Supplementary Table S1**. The RBC was immersed in the center of a quiescent fluid domain ($40 \times 40 \times 40$ µm), with a fluid density and viscosity, 1.0 g/cm^3 and 0.0012 Pa·s, respectively. The uniaxial force was gradually applied at the two end of the RBC. The uniaxial and transverse RBC diameters were captured by the IFEM simulation.

In the **Supplementary Fig. S1b** and **c**, the discharge hematocrit and relative apparent viscosity were respectively calculated to check for the proper RBC intracellular interactions, as induced by blood flow in a narrow microvessel. Experimental observations[5] and computational data[6] show the same trends as the current simulation results. The RBCs were modeled as described in the Method of this manuscript, using the parameters of **Table 1** and **Supplementary Table S1**. The RBCs were immersed in the fluid domain (20×60 µm), with a fluid density and viscosity, 1.0 g/cm^3 and 0.0012 Pa·s, respectively. The maximum velocity of the parabolic profile at the inlet was 1.0 mm/s. The discharge hematocrit (H_d) was calculated following the definition[6]

$$H_d = \frac{\bar{v}_c}{\bar{v}} H_t \quad , \tag{1}$$

where $\bar{v} = Q/A$, and $\bar{v}_c$ is the average cell velocity. On the other hand, the relative viscosity (η_{rel}) is defined as[6]

$$\eta_{app} = \frac{\pi \Delta P D^4}{128 Q L} \quad , \tag{2}$$

$$\eta_{rel} = \frac{\eta_{app}}{\eta_s} \tag{3}$$

where η_{app} is the apparent viscosity, ΔP is the pressure drop, D is the tube diameter, Q is the flow rate, L is the tube length and η_s is the solvent viscosity. The relative viscosity was calculated in the IFEM simulation at 15, 30, and 45% hematocrits.

Finally, in the **Supplementary Fig. S1d**, the thickness of cell free layer predicted with IFEM simulations was compared with experimental and computational results demonstrating a very good agreement, particularly at physiologically relevant hematocrits[6-8.] The RBCs were modeled as described in the Method of this manuscript, using the parameters described in the **Table 1** and **Supplementary Table S1**. The RBCs were immersed in the fluid domain (20 × 60 µm), a fluid density and viscosity, 1.0 g/cm^3 and 0.0012 Pa·s, respectively. The cell free layer was measured at 15, 30 and 45 % hematocrit by averaging, along the channel length, the value for the separation distance between the outer boundary of the RBC clusters and the capillary wall.
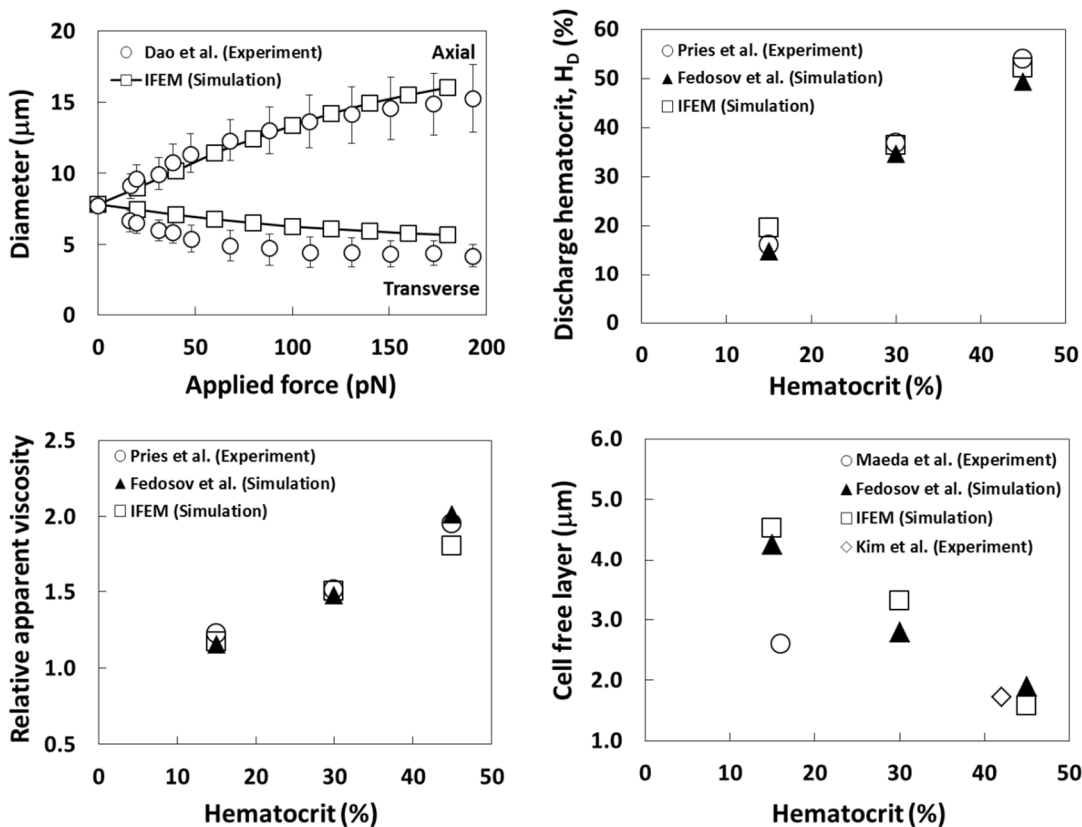

**Supplementary Figure S1** Experimental validation of IFEM for whole blood flow.

NMP trajectories at different hematocrit levels. The IFEM was used to analyze the trajectories of 100 nm and 1,000 nm NMPs in a capillary with different RBC volumetric concentrations, namely 0, 15 and 30% hematocrit. These are shown in the **Supplementary Fig. S2** and S**3** for the 100 nm and 1,000 nm NMPs, respectively. As expected, in the absence of RBCs (0% hematocrit), the NMPs follow a straight trajectory along the streamlines with no appreciable lateral drifting. Differently, at 15 and 30% hematocrit, a lateral motion is observed with a trajectory deviating away and towards the midline. The largest and more rapid fluctuations in lateral motion were observed for the small NMPs (100 nm in diameter), at the lower hematocrit (15%). Indeed, with a lower RBC volumetric concentration, the separation distance between adjacent cells is larger and NMPs can more easily move through the circulating cells, thus leading to a more hectic NMP dynamics. Overall, these data demonstrate that larger, submicron to micron-sized NMPs can be more efficiently excluded by the vessel core, pushed laterally by the fast moving RBCs; whereas the smaller NMPs would benefit far less from this exclusion mechanisms and would stay confined within the vessel core for longer times.
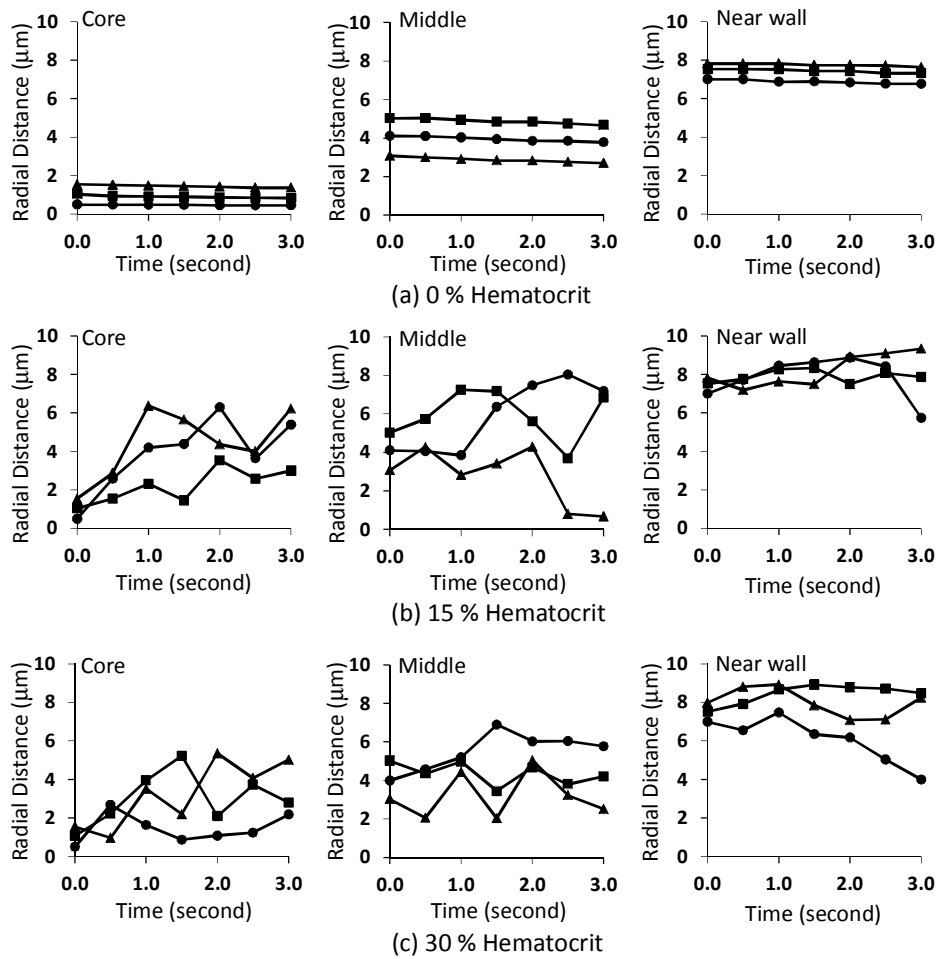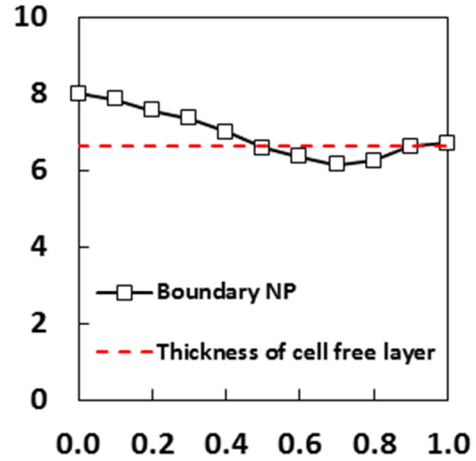

Supplementary Figure S2 Trajectories for 100 nm NMPs in a capillary with different hematocrits, namely 0, 15 and 30%.
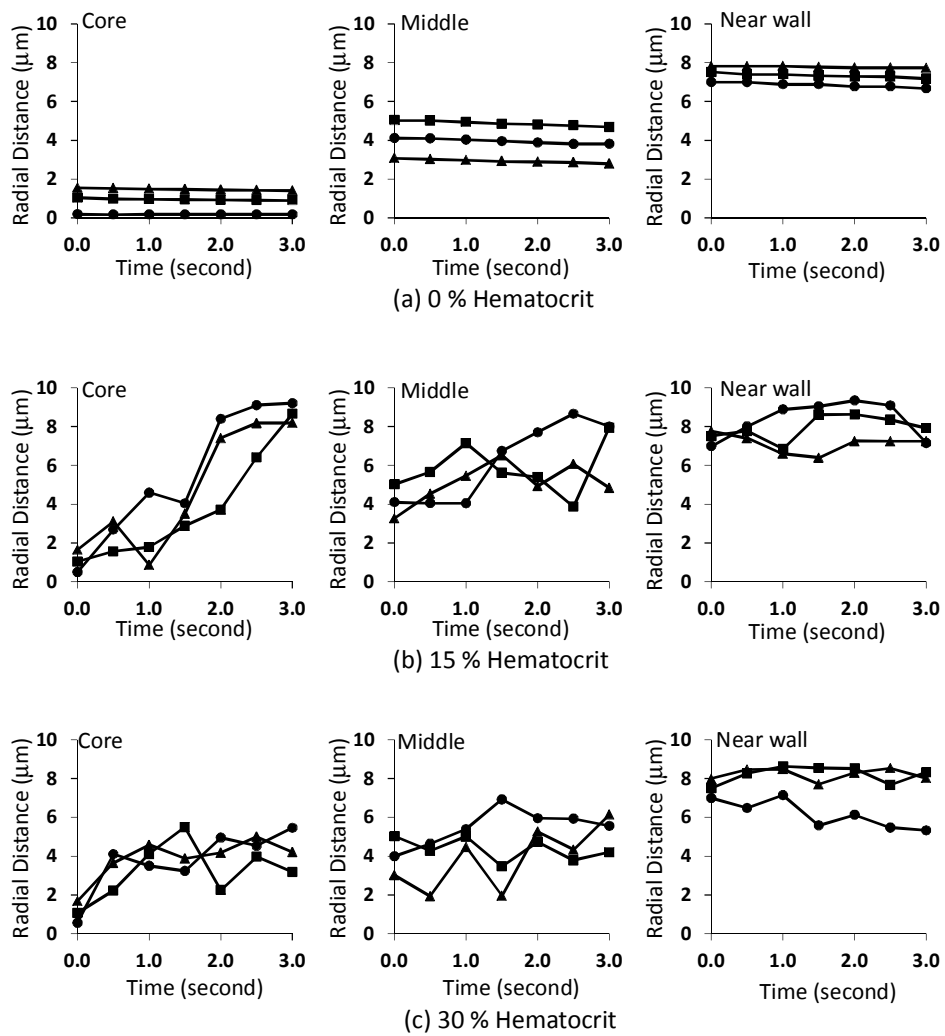
Supplementary Figure S3 Trajectories for 1,000 nm NMPs in a capillary with different hematocrits, namely 0, 15 and 30%.
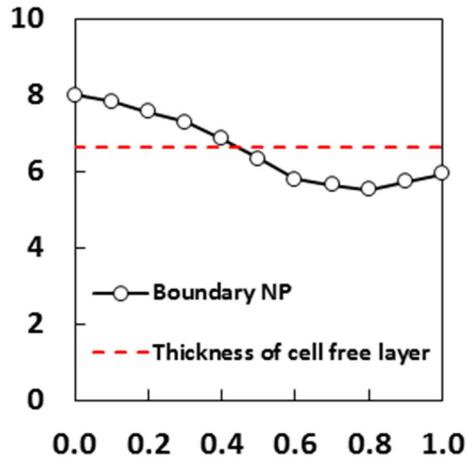
(a) 10 nm **(b) 50 nm**

Supplementary Figure S4 Re-entering NMPs to the RBC core region. Particles are re-entered from cell free layer to blood flow stream when they have diameters 10 nm and 50 nm at 30% hematocrit.

Intravital two-photon microscopy analysis. With comparable optical resolution to confocal microscopy, two-photon microscopy offers deeper optical access to biological tissues by using near-infrared wavelength which has less scattering and absorption. The use of low energy photons also reduces photodamage to the tissue. As the two-photon absorption is nonlinear process depending on I^2, with I being the light intensity, intrinsic optical sectioning for three dimensional imaging is achieved by spatiotemporal light focusing without a pinhole. Due to these benefits, two-photon microscopy is currently gold-standard for microscopic in vivo imaging in various biomedical studies especially in neuroscience, immunology, and vascular biology.[9]
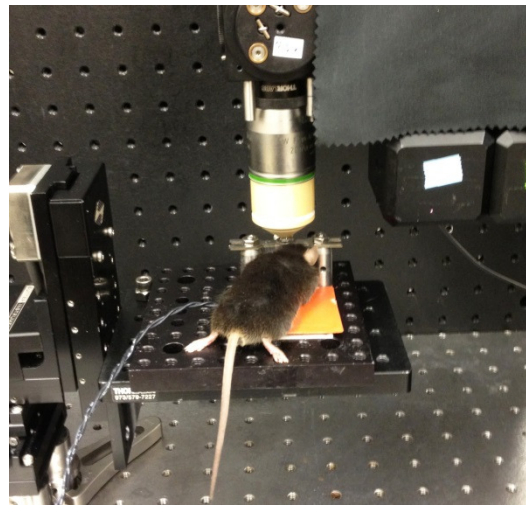
A
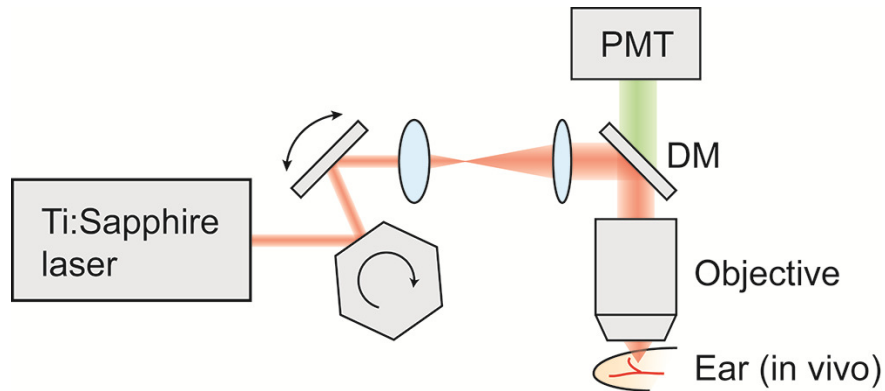
B
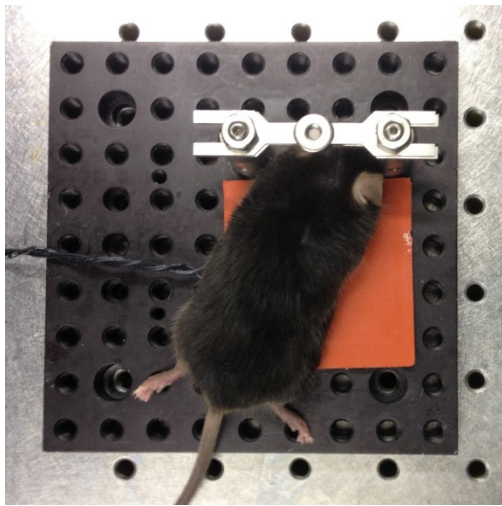
c

Supplementary Figure S5 Intravital two-photon microscopy setup. a) Schematics of a video-rate two-photon microscopy. This system achieves a frame rate of 30 Hz with a rotating polygon mirror. DM, dichroic mirror. PMT, photomultiplier tube. **b, c**) Photographs of a mouse prepared for imaging the ear. The ear is glued on the bottom plate and sandwiched by the top metal plate with a glass opening. The ear is imaged with a 20X, NA1.0 water immersion objective lens.

Supplementary Movie S1 Intravital microscopy analysis of the vascular transport for 200 nm beads. The movie shows the dynamics of 200 nm spherical beads (yellow dots) transported within the ear microcirculation of a mouse. The beads appear to follow the streamlines and distribute quite uniformly within the longitudinal cross section of the vessel. At times, larger aggregates are seen, clearly moving in proximity of the vessel walls. (image size 250 × 250 µm)

Supplementary Movie S2 Intravital microscopy analysis of the vascular transport for 1,000 nm beads. The movie shows the dynamics of 1,000 nm spherical beads (yellow dots) transported within the ear microcirculation of a mouse. The beads appear to mostly move in proximity of the vessel walls. (image size 250 × 250 µm)

Supplementary Movie S3 Whole blood flow at 15% hematocrit. The motion of RBCs within a capillary is shown for a sub-physiological value of the hematocrit (15%). The deformation of the RBC and the implementation of the periodic boundary conditions between the outlet and inlet cross sections are clearly demonstrated.

Supplementary Movie S4 Whole blood flow at 30% hematocrit with NMPs. The motion of RBCs and the transport of 100 nm spherical beads (yellow dots) within a capillary are presented. These smaller nanoparticles are shown to move with the RBCs with little lateral drifting.

REFERENCES

1. Lee, T.-R._, et al._ Immersed finite element method for rigid body motions in the incompressible Navier–Stokes flow. _Computer methods in applied mechanics and engineering_ 197, 2305-2316 (2008).
2. Liu, Y. & Liu, W.K. Rheology of red blood cell aggregation by computer simulation. _Journal of Computational Physics_ 220, 139-154 (2006).
3. Zhang, L., Gerstenberger, A., Wang, X. & Liu, W.K. Immersed finite element method. _Computer methods in applied mechanics and engineering_ 193, 2051-2067 (2004).
4. Dao, M., Lim, C.T. & Suresh, S. Mechanics of the human red blood cell deformed by optical tweezers. _J Mech Phys Solids_ 51, 2259-2280 (2003).
5. Pries, A.R._, et al._ Resistance to Blood-Flow in Microvessels in-Vivo. _Circ Res_ 75, 904-915 (1994).
6. Fedosov, D.A., Caswell, B., Popel, A.S. & Karniadakis, G.E. Blood Flow and Cell-Free Layer in Microvessels. _Microcirculation_ 17, 615-628 (2010).
7. Maeda, N., Suzuki, Y., Tanaka, S. & Tateishi, N. Erythrocyte flow and elasticity of microvessels evaluated by marginal cell-free layer and flow resistance. _Am J Physiol-Heart C_ 271, H2454-H2461 (1996).
8. Kim, S., Kong, R.L., Popel, A.S., Intaglietta, M. & Johnson, P.C. Temporal and spatial variations of cell-free layer width in arterioles. _Am J Physiol-Heart C_ 293, H1526-H1535 (2007).
9. Kim, J.K._, et al._ Fabrication and operation of GRIN probes for in vivo fluorescence cellular imaging of internal organs in small animals. _Nature protocols_ 7, 1456-1469 (2012).